Role of black carbons mass size distribution in the direct aerosol radiative forcing

Gang Zhao[1], Jiangchuan Tao[2], Ye Kuang[2], Chuanyang Shen[1], Yingli Yu[1], Chunsheng Zhao[1*]

[1]Department of Atmospheric and Oceanic Sciences, School of Physics, Peking University, Beijing, China

[2]Institute for Environmental and Climate Research, Jinan University, Guangzhou 511443, China

[*]***Correspondence to: Chunsheng Zhao (zcs@pku.edu.cn)***

Abstract

Large uncertainties exist when estimating radiative effects of ambient black carbon (BC) aerosol. Previous studies about the BC aerosol radiative forcing mainly focus on the BC aerosols' mass concentrations and mixing states, while the effects of BC mass size distribution (BCMSD) were not well considered. In this paper, we developed a method by measuring the BCMSD by using a differential mobility analyzer in tandem with an aethalometer. A comprehensive method of multiple charging corrections was proposed and implemented in measuring the BCMSD. Good agreement was obtained between the BC mass concentration integrated from this system and that measured in bulk phase, demonstrating the reliability of our proposed method. Characteristics of the BCMSD and corresponding radiative effects were studied based on field measurements conducted in the North China Plain by using our own designed measurement system. Results showed that the BCMSD had two modes and the mean peak diameters of the two modes were 150 nm and 503 nm respectively. The BCMSD of coarser mode varied significantly under different pollution conditions with peak diameter varying between 430 nm and 580 nm, which gave rise to significant variation in aerosol buck optical properties. The aerosol direct aerosol radiative forcing was estimated to vary by 8.45% for different measured BCMSDs of coarser mode, which shared the same magnitude to the variation associated with assuming different aerosol mixing states (10.5%). Our study reveals that the BCMSD matters as well as their mixing state in estimating the direct aerosol radiative forcing. Knowledge of the BCMSD should be fully considered in climate models.

1 Introduction

Atmospheric black carbon (BC) is the second strongest absorbing components in atmosphere (Bond et al., 2013) but the magnitudes of the warming effects are poorly quantified. When emitted to the surrounding, BC particles transform the morphology from fractal to spherical and then grow as fully compact particles with other components depositing on the BC aerosol (Peng et al., 2016). The

variation in the shapes of BC aerosols, together with the variation in the mixing states, can lead to substantial change of aerosol optical properties (Liu et al., 2017;China et al., 2013;Wu et al., 2016a;Wu et al., 2018). BC aerosols also have significant influence on the climate by interacting with clouds (Koch and Del Genio, 2010;Roberts et al., 2008;Stevens and Feingold, 2009), ice and snow (Bond et al., 2013). Recent study shows that the solar absorption of BC can suppress the turbulence in the atmospheric boundary layer (Wilcox et al., 2016). It is found that BC emissions may be responsible for the incensement of droughts and floods in China and India (Menon et al., 2002). In addition, BC can pose a serve threat to human health through inhalation (Nichols et al., 2013;Janssen et al., 2011).

Comprehensive studies have been carried out to evaluate the climate effect of BC based on the measurement of BC mass concentrations (m_{BC}) (Koch et al., 2009;Ramanathan and Carmichael, 2008). The m_{BC} near the ground have been well characterized (Ramachandran and Rajesh, 2007;Ran et al., 2016b;Reddington et al., 2013;Song et al., 2013), and the BC vertical distributions are widely measured and evaluated as well (Ran et al., 2016a;Babu et al., 2011;Ferrero et al., 2011). Despite these measurements, more insights into the BC microphysical properties can help to estimate the influence of BC aerosols on visibility (Zhang et al., 2008), climate (Jacobson, 2001) and human health (Lippmann and Albert, 1969). These microphysical properties include BC morphology (Zhang et al., 2016), density (Zhang et al., 2016), complex refractive index (Bond et al., 2013), hygroscopicity (Zhang et al., 2008;Peng et al., 2017), mixing states (Moffet et al., 2016;Raatikainen et al., 2017), and particularly, the mass size distribution (BCMSD) (Cheng et al., 2012;Cheng and Yang, 2016;Gong et al., 2016). Knowledge of BCMSD is not only helpful to study the mixing state of BC aerosols (Raatikainen et al., 2017), but also essential to model the role of BC in evaluating regional and global climate accurately. BC radiative effects is highly sensitive to the emitted BC particle size distribution (Matsui et al., 2018). The health impacts of BC are significantly related to BCMSD (Turner et al., 2015). Furthermore, the information of BCMSD can help to study the source, the evolution and the mixing state of ambient BC aerosols (Yu et al., 2010).

Many methods have been proposed to measure the BCMSD. For instance, the BCMSD was measured by sampling the aerosol in the size range from about 50 nm to several micrometers onto quartz fiber filter substrates using a micro-orifice uniform deposit impactor (MOUDI) (Venkataraman and Friedlander, 1994;Guo, 2016). Cheng et al. (2014) developed a method to

measure the BCMSD by employing two aethalometers in parallel, with one to measure total m_{BC} and the other to measure m_{BC} below specific particle sizes using a size cut-off inlet. The above two methods measure the BCMSD corresponding to the aerodynamic diameter. The Single Particle Soot Photometer (SP2) is developed and widely used because it provides sing particle information, hence the BCMSD and the mixing state of the atmospheric aerosols can be derived directly (Schwarz et al., 2006;Gao et al., 2007;Huang et al., 2012;Singh et al., 2016). The BCMSD corresponding to the ambient aerosol mobility diameter can be measured by using a differential mobility analyzer (DMA) in tandem with SP2 (Raatikainen et al., 2017). However, the laser-induced incandescence method cannot provide reliable information about the particles beyond the range of 70 nm and 400 nm (Moteki and Kondo, 2010), which results in the lack of the knowledge of the BCMSD characteristics for these aerosols over 400 nm. The results from MOUDI find that a great amount of BC locates at the aerodynamic diameter range of between 370 and 1000 nm (Hu et al., 2012;Huang and Yu, 2008). However, the measurements of MOUDI cannot give detailed information of the BCMSD evolution due to the low temporal and diameter resolution (Hu et al., 2012;Huang and Yu, 2008). The characteristics of the BCMSD larger than 370 nm is not well studied due to the limitation of the instrument.

Recently, Ning et al. (2013) and Stabile et al. (2012) proposed a new method to measure the BCMSD by using differential mobility analyzer (DMA) in tandem with Aethalometer (AE). This method has the potential of measuring the BCMSD from 20 nm to 584 nm with high time resolution. We develop and validate the BCMSD measurement system based on the works of Ning et al. (2013). The developed measurement system was employed in a field campaign in the North China Plain. The characteristics of the measured BCMSD were studied based on the field measurement. Furthermore, the effects of BCMSD variations on the aerosol optical properties and corresponding direct aerosol radiative properties were evaluated. The aerosol optical properties were calculated by using the Mie scattering theory. The direct aerosol radiative forcing (DARF) were estimated by using the Santa Barbara DISORT (discrete ordinates radiative transfer) Atmospheric Radiative Transfer (SBDART) model.

The structure of this paper are organized as follows. Section 2 gives the information about the instrument setup and field measurement. Section 3 gives the detailed method used in this study, which contains: 1, conducting multiple charging corrections when deriving the aerosol BCMSD and

2, evaluating the aerosol optical and radiative properties for different BCMSD. Results and discussions are shown in section 4. The conclusion is drawn in the last part.

2 Instrument Setup

The measurement system setup was based on the works of Stabile et al. (2012) and Ning et al. (2013) as schematically shown in Fig.1. The ambient sample aerosol particles were firstly dried to below relative humidity of 30% through a Nafion drying tube before passing through to the DMA (Model 3081, TSI, USA). The DMA scanned aerosol particles with diameter ranges from 12.3 to 697 nm over a period of 285 seconds and started another scanning after a pause of 15 seconds, so one complete cycle took 5 minutes. The sheath and sample flow rates of the DMA were 3 lpm and 0.5 lpm, respectively. The quasi-monodisperse aerosols that passed through the DMA were further divided into two flows: with one lead to an aethalometer (AE51, Model 51, MicroAeth, USA) with a flow rate of 0.2 lpm to measure the absorption coefficient (σ_{abs}) at 1 second time resolution; and the other one with flow rate of 0.3 lpm flow directed to a CPC (Model 3772, TSI, USA), which counted particle number concentrations at 0.1 second resolution. Clean air with a flow rate of 0.7 lpm was used to compensate for the CPC inlet flow, which had default flow rate of 1 lpm. Overall, the combination system of DMA, CPC and AE51 could provide one PNSD and size-resolved σ_{abs} scan every 5 minutes. If the mass absorption coefficient (MAC) at a given diameter is known, the BCMSD can be derived correspondingly.

An aethalometer (AE33, Model 33, Magee, USA) was used to measure the σ_{abs} or m_{BC} with a time resolution of 1 minute. The mass concentration of particles with diameter smaller than 2.5 μm (PM2.5) was concurrently measured with time resolution of 1 minute during the filed observations by the Tapered Element Oscillating Microbalance (TEOM) Dichotomous Ambient Particulate Monitor (1405-DF), which was an indicator of the pollution conditions.

From 21 March to 9 April in 2017, an intensive field measurement was conducted to characterize of the ambient dry aerosol BCMSD corresponding to aerosol mobility diameter at the AERONET BEIJING_PKU station (N39°59′, E116°18′). This station was located on one roof of Peking University campus in the north west of Beijing, China. There were two main streets, Chengfu Road to the south and Zhongguancun Street to the west that surrounding the station. The aerosol sampled at this station were mainly composed of urban roadside aerosols (Zhao et al., 2018).

3 Methodologies

3.1 Retrieving the BCMSD

Five steps were involved to calculate the BCMSD using the raw data from the measurement system: 1), correcting the 'loading effect' and 'multiple scattering effect' of σ_{abs} measured by AE51; 2), matching the instrument time between the AE51 and CPC; 3), matching the measured $\sigma_{abs}$and diameter to get the raw size-resolve σ_{abs} that is not involved in multiple charging corrections; 4), conducting the multiple charging corrections of the measured raw size-resolved σ_{abs}; 5), transforming the size-resolved σ_{abs} into BCMSD.

3.1.1 Obtaining the raw size-resolved σ_{abs}

The aethalometer (AE51 and AE33) is a well-developed and widely used instrument to measure the σ_{abs} (Drinovec et al., 2015;Hansen et al., 1984). When absorbing aerosols accumulates on the sample filter of the aethalometer continuously, the σ_{abs} can be determined by concurrently measuring the light intensities I after the fiber filter and the light intensities I_0 transmitted through reference spot which is free of aerosol loading. The light attenuation (ATN) is defined as:

$$\mathrm{ATN} = 100 \cdot \ln(\frac{I_0}{I}). \quad (1)$$

The total σ_{abs} of the loaded particle on the filter is given by:

$$\sigma_{abs,tot} = \frac{\mathrm{A}\cdot\mathrm{ATN}}{100}, \quad (2)$$

where A is the sample spot area on the filter. The instantaneous σ_{abs} can be calculated through the increment of $\sigma_{abs,tot}$:

$$\sigma_{abs} = \frac{\sigma_{abs,tot}}{\Delta t} = \frac{A\cdot\Delta ATN}{100\cdot F\cdot\Delta t}, \quad (3)$$

where F is the flow rate and ΔATN is the ATN variation during the time period of Δt. The $\sigma_{abs,tot}$ can be transformed to m_{BC} when the mass attenuation cross-section (MAC) of BC is known. Traditionally, a constant MAC at 7.7 g/m^2 was used to deduce the m_{BC} (Drinovec et al., 2015).

Corrections of the measured σ_{abs} are necessary because the systematic bias exists due to the prevailingly known 'loading effect' and multiple scattering effect (Drinovec et al., 2015;Virkkula et al., 2015;Virkkula et al., 2007). The AE33 can directly provide the corrected σ_{abs} values through measuring two light intensities of two spots with different BC load efficiencies (Drinovec et al., 2015). For AE51, The correcting method in Virkkula et al. (2007) was adopted:

$$\sigma_{abs,\ corrected} = (1 + \mathrm{k} \times ATN)\sigma_{abs,uncorrected}, \quad (4)$$

where k is the correction factor and a constant value of 0.004 is employed in this study to correct the σ_{abs} from AE51. In the first part of the supplementary material, we showed that the loading effects corrections of $\sigma_{abs}$from AE51 were essential and the value of $\sigma_{abs}$from AE33 could be used as a reference for the measured BCMSD. As for the multiple scattering corrections, Zhang et al. (2018) compared the measured σ_{abs} measured by AE33 and by Multi-Angle Absorption Photometer (MAAP) at Tsinghua University, which is about 2 km away from our measurement site. They recommended a compensation factor of 2.6 to be used and we adopted the same factor in our study.

Time correction was needed because time gaps between voltages implied on the DMA (particle size) and sample particles measured by different instruments were not the same. The time correction procedures were conducted every day during the field measurement to ensure that the time deviations of the CPC and the AE51 were constrained within 2 seconds.

Fig. S3 gave the time series diagram of scanned aerosol diameters by DMA, measured σ_{abs} from AE51, and the aerosol number concentrations counted by CPC. The aerosol PNSD (or size-resolved σ_{abs}) could be calculated by matching the DMA diameter and the measured aerosol number concentrations (or measured $\sigma_{abs}$by simply using the single particle charge ratio for each electrical mobility diameter. These measured PNSD and size-resolved σ_{abs} did not consider the effect of multiple-charging corrections and are labeled as raw aerosol PNSD and raw aerosol size-resolved σ_{abs}.

3.1.2 Multiple charging corrections of raw size-resolved σ_{abs}

In the work of Ning et al. (2013) study, lots of efforts were made to evaluate the performance of the instrument. They considered the diffusion corrections and particle charging corrections. However, the particle charging corrections were limited to single particle charge ratio as they mentioned that they simplified the particle charge correction by applying the peak electrical mobility for the calculation of representative particle size for each mobility bin and single particle charge ratio for each primary mobility. They ignored the fact that the aerosol samples selected by the DMA were quasi-monodisperse with different charges and different diameters.

We proposed a new algorithm for the multi-charge corrections of the size-resolved σ_{abs}. Multi-charge corrections to the measured size distribution were prevailing when the DMA was used to scan the aerosol sizes. When the DMA and CPC are used together to measure the aerosol particle number size distribution (PNSD), the multi-charging corrected aerosol PNSD can be significantly

different from the raw measured one (Bau et al., 2014;He and Dhaniyala, 2013;He et al., 2015). As shown in the results part of this study, the multi-charge corrections of the size-resolved σ_{abs} could cause differences in both the magnitude and shape of the size-resolved σ_{abs}. Therefore, it is necessary to perform multi-charge corrections on the size-resolved σ_{abs}. This study developed a new algorithm to correct the size-resolved $\sigma_{abs}$from measured value based on the work of Hagen and Alofs (2007) and Deng et al. (2011).

When the DMA is charged with a negative voltage, those aerosols with a small range of electrical mobility (Z_P) can pass through the DMA:

$$Z_P = \frac{q_{sh}}{2\pi VL}\ln(\frac{r_1}{r_2}), \quad (5)$$

where q_{sh} is the sheath air flow rate; V is the average voltage on the inner center rod; r_1 and r_2 are the outer and inner radius of annular space respectively. The Z_P is related with D_p by elementary charge (e), number of elementary charges on the particle (n), and gas viscosity poise (μ) with:

$$Z_p = \frac{neC(D_p)}{3\pi\mu D_p}, \quad (6)$$

where $C(D_p)$ is Cunningham slip correction:

$$\mathrm{C} = 1 + \frac{2\tau}{D_p}(1.142 + 0.558e^{-\frac{0.999D_p}{2\tau}}), \quad (7)$$

where τ is the gas mean free path. From equation 7, aerosol particles can have the same Z_P despite that they have different n and D_p. At the same time, there exists a relatively larger portion of multiple charged particles for those particles with diameters between 100 nm and 400 nm when the ambient aerosols pass through the X-ray (Tigges et al., 2015;Wiedensohler and Fissan, 1988). Through the above discussion, the selected aerosols by DMA at a given electrical mobility can have different charges which will correspond to different diameters.

When the scan diameter is set as Dp_i for the singly charged particles and the respective voltage of DMA is $\mathrm{V_i}$ (i =1, 2, …, I), aerosol particles with electro-mobility of $\mathrm{Z_{p,i}}$ (i=1, 2, …, I) can pass through the DMA and the observed σ_{abs} by AE51 can be expressed as:

$$R_i = \int_0^\infty G(i,x)A(x)n(x)dx, \quad (8)$$

where x is the scale parameter, with the definition of $\mathrm{x} = \log(\mathrm{Dp}_i)$, A(x) is the average$\sigma_{abs}$ of single particle for scale parameter x, and $\mathrm{n(x)} = \mathrm{dN/dlogDp}$ is aerosol PNSD that is the multiple

charging corrected results from the measured aerosol PNSD. We define the kernel function G (i, x), which is crucial to the algorithm, as:

$$G(i,x) = \sum_{v=1}^{\infty} \emptyset(x,v)\Omega(x,v,i), \quad (9)$$

where $\emptyset(x,v)$ is the probability of particles that are charged with v charges at the scale parameter of x (Wiedensohler, 1988). $\Omega(x,v,i)$ is the probability of particles that can pass through the DMA with v charges at the scale parameter x (Knutson and Whitby, 1975). In this study, the maximum value of v is 10.

The multiple charging corrections can be expressed as computing the $A(x_i^*)$, in which x_i^* is the predetermined scale parameter from the DMA. To get the numerical integration results of equation 9, the diameter interval that is 1/50 of the measured diameter is used. Thus, equation 9 can be written as

$$R_i = \int_0^{\infty} G(i,x)A(x)n(x)dx = \Delta x_i \sum_{j=1}^{50} \beta_j G\left(i, x_{i,j}\right)A\left(x_{i,j}\right)n(x_{i,j}), \quad (10)$$

where $\beta = \begin{cases} 0.5, & j = 1, J \\ 1, & otherwith \end{cases}$; $x_{i,j}$ is the j^{th} (j=1 ,2 ,…, 50) parameter that locates at the parameter x_i and x_{i+1} and $A\left(x_{i,j}\right)$ (i=1, 2, …, I; j=1, 2, …, 50), the BC mass ratio at scale parameter $x_{i,j}$, is expressed as the linear interpolation of the values at the measured diameters.

$$A\left(x_{i,j}\right) = A(x_i) + P_i(x_{i,j} - x_i), \quad (11)$$

where P_i is the slope of the linear interpolation result of

$$A(x_k^*) = C + P_i \cdot x_k^*. \quad (12)$$

x_k^* refers to these five diameters that are nearest to the predetermined scale parameter x_i. C is the intercept of the linear interpolation result.

With $H_{i,j} = \beta_j \Delta x_i G\left(i, x_{i,j}\right)n(x_{i,j})$, equation 11 can be written as

$$R_i = \sum_{j=1}^{J} H_{ij}\left[A(x_i) + P_i\left(x_{i,j} - x_i\right)\right] = \sum_{j=1}^{J} H_{ij}A(x_i) + \sum_{j=1}^{J} H_{ij}\,P_i x_{i,j} - \sum_{j=1}^{J} H_{ij}\,P_i x_i$$

$$= \sum_{k=1}^{I}\left(\sum_{j=1}^{J} H_{ij}\,\delta(\mathrm{i}-\mathrm{k})\right)\mathrm{A}(x_k^*)) + \sum_{k=1}^{I}\left(\sum_{j=1}^{J} H_{ij}\,x_{i,j}\delta(\mathrm{i}-\mathrm{k})\right)\mathrm{P}_k - \sum_{k=1}^{I}\delta(\mathrm{i}-\mathrm{k}))P_k x_k^*$$

$$= \sum_{k=1}^{I} Q_{ik}A(x_k^*) + \sum_{k=1}^{I} T_{ik}P_k - \sum_{k=1}^{I} Q_{ik}P_k x_k^*, \quad (13)$$

where $\delta(x) = \begin{cases} 0, x \neq 0 \\ 1, x = 0 \end{cases}$,

$$Q_{ik} = \sum_{j=1}^{J} H_{ij}\delta(i-k), \quad (14)$$

and $T_{ik} = \sum_{j=1}^{J} H_{ij}x_{i,j}\delta(i-k)$. (15)

By letting the

$$S_i = R_i - \sum_{k=1}^{I} T_{ik} P_k + \sum_{k=1}^{I} Q_{ik} P_k x_k^*. \quad (16)$$

This equation is then expressed as

$$S_i = \sum_{k=1}^{I} Q_{ik} A(x_k^*), \quad (17)$$

or

$$S = QA, \quad (18)$$

where S and A are $I \times 1$ vectors and Q is an $I \times I$ matrix. This matrix can be solved by using the non-negative least square method.

Finally, the A(x) can be determined and the corresponding size-resolved σ_{abs} that is multiple charging corrected can be calculated.

3.1.3 Transform the size-resolved σ_{abs} into BCMSD

MAC of different size range is necessary when transform the size-resolved σ_{abs} into BCMSD. The MAC at different size should be different. When the size-resolved σ_{abs} is converted into BCMSD with a constant MAC, the derived BCMSD would be biased.

The size-resolved MAC was calculated using the Mie scattering model (Bohren and Huffman, 2007). Based on the Mie scattering theory, MAC values vary for different aerosol core diameter and different total diameter. Results from SP2 measurement show that the size distribution of the BC core diameter peaked at around 120 nm in Beijing (Zhang et al., 2017). For each aerosol diameter, the MAC value with core diameter of 120 nm was used to transform the BCASD into the BCMSD. MAC values with core diameter at 120±15 nm were calculated and shown in Fig. 2. From Fig. 2, the MAC varied significantly between 3.6 and 9.2 m^2/g. The constant MAC values 7.7 m^2/g corresponded to the aerosol diameter of 269 nm. The calculated mean MAC values in Fig. 2 under different diameter were used in this study.

3.1.4 Validation of the multiple charging corrections

An example of the multiple charging corrections of the size-resolved σ_{abs} was shown in Fig. 3. The corrections of aerosol PNSD were based on the work of Hagen and Alofs (2007). As shown in Fig. 2(a), the corrected aerosol PNSD was significantly different from the original uncorrected one. There were about half of the measured particles have multiple elementary charge in the size range between 100 and 200 nm. The raw uncorrected aerosol PNSD had a peak value of 10920 cm^{-3} at 98 nm while the corrected aerosol PNSD reached its peak value of 8450 cm^{-3} at 98 nm. The peak

positions of the raw aerosol particle mass size distribution (PMSD, dm/dlogDp) peaked at 322 nm with a peak value of 86.3 μg/m^3 and the corrected aerosol PMSD had a peak value of 53 μg/m^3 at 461 nm. The peak position of the aerosol PMSD shifted a lot before and after the multiple charging corrections. The similar case for the size-resolved σ_{abs} was shown in Fig. 2(b). The shape of size-resolved σ_{abs} had changed substantially due to the multiple charging corrections. The measured raw BCMSD had a peak diameter near 320 nm and the magnitude of size-resolved σ_{abs} plateau reached 34.3 Mm^{-1}, which was in accordance with the results of Ning et al. (2013), where the multiple charging corrections were not involved. However, the corrected size-resolved σ_{abs} peaks near 410 nm, with a peak value of about 29.5 Mm^{-1}. According to the result, a small amount of σ_{abs} remained in particles with diameter between 100nm and 200nm. The measured size-resolved σ_{abs} changed a lot when multiple charging corrections were implemented, which highlighted the necessity of implementation of appropriate multiple charging corrections

The σ_{abs} integrated from measured size-resolved σ_{abs} changed after multiple charging corrections. Fig. S4 showed the comparison results of the σ_{abs} measured by AE33 and the σ_{abs}integrated from AE51 measurements. The σ_{abs} integrated from uncorrected and corrected size-resolved σ_{abs} versus σ_{abs} measured by AE33 were shown in Fig.S4(a) and Fig.S4(b), respectively. Before multiple charging corrections, the σ_{abs} from uncorrected size-resolved σ_{abs} increased linearly with the σ_{abs} from AE33, with R^2 equaling 0.87, but it was 2.37 times that of AE33 in average. As a comparison, overall magnitude of σ_{abs} integrated from corrected size-resolved σ_{abs} agreed better with that from AE33 with a slope of 1.2. With the discussion above, multiple charging corrections were essential for size-resolved σ_{abs} and BCMSD measurements.

3.2 Fitting the BCMSD by using two log-normal models

Based on the measurement results, the BCMSD had two modes for most of the conditions. The BCMSD are assumed to be of two log-normal distributions as:

$$m_{fit,Dp} = \sum_{i=1,2} \frac{m_i}{\sqrt{2\pi}\log(GSD_i)} \cdot \exp\left(-\frac{\left[\log(D_p)-\log(D_{m,i})\right]^2}{2log^2(GSD_{,i})}\right), \quad (19)$$

Where D_p is the diameter of the aerosols; m_i is the mass of mode i (i=1,2); GSD_i is the geometric standard deviation at mode i (i=1,2), and $D_{m,i}$ is the geometric mean diameter of the mode i (i=1,2). The GSD_i and $D_{m,i}$ can be determined by using the least square method with the objective function as :

$$J = \sum_{i=1,n}\left(m_{Dp_i} - m_{fit,Dp_i}(D_{m1}, GSD_1, D_{m2}, GSD_2)\right)^2, \qquad (20)$$

Where m_{Dp_i} is the measured mass distribution at Dp_i, while m_{fit,Dp_i} is the fit mass distribution at Dp_i.

3.3 Estimating aerosol optical properties with different BCMSD

The Mie scattering model was used to study the influence of the BCMSD variation on the aerosol optical properties. When running the Mie model, aerosol PNSD and BC were necessary. In this study, The BCMSD was assumed to be log-normal distributed. D_m of the BCMSD was set to vary from 100 nm to 600 nm. Geometric standard deviation (GSD) of the BCMSD was set to be in the range between 1.3 and 1.8. BC was treated as partially externally mixed and the remaining aerosols was treated as core-shell mixed. The ratio of externally mixed m_{BC} to core-shell m_{BC} was determined by the method introduced in Ma et al. (2012) and a mean ratio of 0.51 was used. The density and refractive index of BC were set as 1.5 g/cm3 and 1.8+0.54i (Kuang et al., 2015), respectively. The complex refractive index of non-absorbing aerosols was 1.53+10-7i (Wex et al., 2002) at the wavelength of 525 nm. More details of calculating the aerosol optical properties by using the aerosol PNSD and BCMSD, can refer to Kuang et al. (2016).

The aerosol PNSD and m_{BC} used here is the mean result of aerosol PNSD and m_{BC} over the whole field measurement respectively. The amount of BC particle adopted in this study is the mean value of the m_{BC} measured by AE33. For each BCMSD, extinction coefficient (σ_{ext}), the scattering coefficient (σ_{sca}), the single scattering albedo (SSA), and the asymmetry factor (g) could be obtained from the output of Mie scattering model.

3.4 Evaluating the DARF with different BCMSD

In this study, the SBDART model (Ricchiazzi et al., 1998) was employed to estimate the DARF. In our study, the instantaneous DARF for cloud free conditions at the top of atmosphere was calculated for irradiance wavelength range from 0.25 to 4 μm. Input of the model required the profiles of aerosol σ_{ext}, SSA, g. These profiles were calculated from the parameterization of the aerosol vertical distributions. Details of calculating the σ_{ext}, SSA and g profiles can refer to part 4 in the supplementary material. In brief, the aerosol σ_{ext}, SSA and g profiles were calculated based on the given aerosol PNSD and BCMSD. The DARF can be estimated using the above aerosol optical profiles.

The aerosol optical properties and the corresponding aerosol optical profiles vary with different BCMSD. Then the DARF should be different for different BCMSD. By estimating the DARF using different aerosol BCMSD, the influence of BCMSD on the aerosol radiative properties can be studied.

4 Results and Discussions

4.1 Measurement results of the BCMSD

The time series of measured PM2.5, aerosol PNSD and BCMSD were shown in Fig. 3. During the observation period, the PM2.5 varied from 0.06 to 220 μg/m^3, with a mean value of 71.5 ± 52.56 μg/m^3. Three periods of heavy PM2.5 loading were observed: (1) PM2.5 increased from around 100 μg/m^3 to 200 μg/m^3 and decreased slowly to 1 μg/m^3 in the period 21-26, March; (2) the PM2.5 accumulated slowly from 28 to 30, March and dissipated quickly from 30, March to 1, April; (3) the rapid accumulation and dissipation of PM2.5 happened during 2 to 5, April. During the last five days, PM2.5 fluctuated between 20 and 120 μg/m^3. For each pollution condition, both the aerosol total number concentrations and the aerosol median diameter increased. The aerosol median diameter varied between 31 nm and 169 nm with a mean value of 78 ± 31 nm.

Our measurements shew that the BCMSD had two modes with the coarser mode ranging between 430 nm and 580 nm in mobility diameter. Many field measurements had revealed that most of the BC mass locates in the aerodynamic diameter range of 320 nm and 560 nm using the MOUDI (Hu et al., 2012;Huang and Yu, 2008). When the aerodynamic diameter was transformed into mobility diameter with assumption a aerosol effective density of 1.3, the measured BC aerodynamic diameter range corresponded to mobility diameter range of 280 nm and 491 nm. Therefore, the measured size range for coarser mode of BCMSD agreed well with the previous measurement.

The measured aerosol in the field site was representative of the urban aerosol. The BC particles emitted by vehicles contributed significantly to the total aerosol BC mass. These BC particles were rarely coated or thinly coated, and the BC core diameter peaked around 120 nm (Zhang et al., 2017). Therefore, the BCMSD of the smaller mode measured in our study corresponded to these uncoated of thinly coated particles.

The total m_{BC} measured by AE33 ranged from 0.1 to 14 μg/m^3 with an average of 5.04 ± 2.64 μg/m^3. Good consistence was achieved between m_{BC} measured by AE33 and m_{BC} calculated from

measured BCMSD as shown in Fig. 3(d).

4.2 Evolution of the BCMSD under different polluted conditions

Log-normal distribution was used to fit each mode of the BCMSD by using the least square method as introduced in section 3.2. For each mode, the geometric mean diameter (D_m) and the geometric standard deviation (GSD) of the BCMSD were studied.

During the measurement period, both D_m and GSD of the two modes had changed significantly as shown in Fig S7. The D_m of first and second mode varied from 139 to 161 nm and from 420 to 597 nm, respectively. The corresponding mean D_m was 151 and 520 nm. The D_m of the two modes was found to be positive correlated in Fig. S7(a). When the pollution was released from the beginning to 27, March, the D_m decreased from 597 to 420 nm and from 160 to 140 nm for the coarser mode and the smaller mode respectively. The BC containing aerosols tended to be aged and grew larger when the air surrounding get polluted.

GSD for the coarser mode and the smaller mode showed very different properties as shown in Fig. S7(b). For the second mode, GSD varied from around 1.49 to 1.68 with a mean value of 1.57. The GSD get decreased with the pollution condition, which indicated that BC containing aerosols tend to accumulate to a small range of diameters during the aging processing. This phenomenon was consistent with the fact that larger particles grew relative slower in diameter because the growth ratio of small aerosol particle is proportion to the negative power of it's diameter. For the first mode, GSD ranged from 1.41 to around 1.86 with a mean value of 1.63. However, GSD of the smaller mode tend to be larger when the surrounding air get cleaner, which might be related to the complex sources of the BC emission. A small amount of fresh emitted BC particles can have substantial influence on the mass size distribution of the smaller mode because the BC concentrations of the smaller mode were small, especially under clean conditions. In general, the GSD of coarser mode was a good indicator of the BC aging process and that of the smaller mode could partially reflect the complex sources of the BC fine particles.

The relationship between the D_m and the GSD for coarser mode was further analyzed by analyzing the distribution of the D_m and GSD. The GSD and D_m had opposite trends as shown in Fig 5. With the increment of the D_m from 420 to 540 nm, the mean value of GSD decreased from around 1.608 to 1.528 while the m_{BC} increased with the D_m. The statistical relationship between D_m and GSD offered a reasonable representation of the BCMSD under different polluted conditions.

In the following work, mean values of the GSD at different D_m were used to for further discussion. The m_{BC} and GSD is positively correlated. The m_{BC} increased from 2.4 to 8.3 μg/m^3 when the D_m increased from 420 to 540 nm.

Note that the GSD get slightly increased with the increment of D_m when D_m was larger than 520 nm. This might be caused by the limit diameter range of BCMSD measuring system which was from 20 to 680 nm. The multiple charge corrections applied to the BCMSD could influence the BCMSD when D_m of the BCMSD was near the end of the scanned diameter and may lead to significant uncertainties to the BCMSD. The measurement results indicated that cases of measured D_m of BCMSD larger than 520 nm were few, demonstrating that this multiple correction effect influenced little on shape of measured BCMSD in most cases.

4.3 Influence of BCMSD variation on the aerosol optical properties

The aerosol optical parameters using the measured mean aerosol PNSD and mean m_{BC} corresponding to different GSD and D_m values were shown in Fig. 6. In Fig. 6(a), the aerosol g varied from 0.603 to 0.627 (variation of 4%). Recent work by Zhao et al, 2017 showed that the aerosol g value in the NCP may vary at a range of 10% due to the change of aerosol PNSD. Aerosol g was more sensitive to D_m when the geometric mean diameter of the BCMSD was lower than 400 nm. However, when the D_m was larger than 400 nm, the g become sensitive to both the D_m and the GSD of BCMSD. Overall, the g varied a little bit (0.02 to 0.609) under the representative conditions during the measurement period. For the aerosol SSA, it was sensitive to the D_m over the whole range as shown in Fig. 6(b). SSA varied between 0.90 and 0.94 under the representative measurement conditions. The σ_{sca} had large changes from 325.6 Mm^{-1} to 364.4 Mm^{-1}. The σ_{sca} was quite sensitive to variations in BCMSD when the D_m was larger than 450 nm as shown in Fig.6c. In addition, variations in σ_{sca} relied more on the variations in D_m when D_m was lower than 400 nm. Within the measurement conditions of BCMSD, the σ_{sca} varied from 328 Mm^{-1} to 345 Mm^{-1}. The measured GSD under different D_m went along with the gradient direction of the σ_{sca}, which mean that the evolution of BCMSD in the atmosphere influenced substantially on σ_{sca}. As for the σ_{abs}, it changed from 24.06 Mm^{-1} to 37.27 Mm^{-1} and the corresponding mass absorption cross section (MAC) was estimated to be in the range of 5.44 to 8.08 m^2/g, suggesting that MAC of the BC aerosols should be carefully studied under different BCMSD conditions.

4.4 Influence of BCMSD on the direct aerosol radiative forcing

The estimated DARF values for different GSD and D_m conditions were estimated. When estimating the DARF, the measured mean aerosol PNSD and mean BC mass concentration were used. The results of estimated DARF were shown in Fig. 7(a). DARF at the surface varied from --4.3 w/m^2 to -3.59 w/m^2 for different BCMSD. Within the measured BCMSD range, the DARF varied from -3.97w/m^2 to -3.67w/m^2, which corresponding to 8.45% of variation. The heating rate within the mixed layer was a powerful indicator of the BC particles' absorbing effects, which may help evaluate the development of the boundary layer. The calculated mean heating rate within the mixed layer changed from 2.16 K/day to 2.65 K/day for different D_m and GSD, as shown in Fig. 7(b). The heating rate with the measured BCMSD range could change from 2.24 to 2.50 with a variation of 11.6%.

Mixing states of BC play significant roles in calculations of aerosol optical properties and estimations of DARF (Jacobson, 2001). As a comparison, we estimated the DARF under different conditions of BC mixing state: (1) internally mixed, (2) externally mixed and (3) core-shell mixed. Table 1 gave the estimated DARF and mean heating rate within the mixed layer under different mixing state conditions. Results showed that the DARF under different BC mixing states conditions may change by 10.50%, which shared the same magnitude with 8.45% variation of DARF caused by BCMSD variations. In addition, the heating rate was estimated to vary by 9.71%. These results highlighted that the BCMSD plays significant roles in variations of aerosol optical properties and estimations of DARF as well as the air heating rate caused by the existence of BC particles. It was recommended that a real time measured BCMSD be used when estimating the aerosol DARF, instead of a constant one. The BCMSD was as important as that of the BC mixing states.

5 Conclusions

Knowledge of the BC microphysical properties especially the size-dependent information can help reduce the uncertainties when estimating the aerosol radiative effects. BCMSD is an important quantity in its own right, being directly and indirectly applicable to determination the sources, aging processes and mixing states of BC aerosols. In this study, the characteristics of BCMSD were studied from the field measurement results by using our own developed measurement algorithm.

The BCMSD measurement system was developed and validated based on the works of Ning et al. (2013) by using differential mobility analyzer (DMA) in tandem with Aethalometer (AE). When deriving the BCMSD, a comprehensive multiple charging correction algorithm was proposed and

implied. This algorithm was validated by closure study between the measured total m_{BC} from AE33 and the m_{BC} integrated from the measured BCMSD using the datasets from field measurements. Results showed that the multiple charging corrections could significantly change the shapes and magnitudes of the raw measured BCMSD. The accurate BCMSD characteristics could be obtained by our proposed method in this paper.

The developed measurement system was employed in a field campaign in the North China Plain from 21 Match to 9 April in 2017. The BCMSD was found to have two quasi-lognormal modes with peaks at around 150 nm and 500 nm, respectively. These two modes were consistent with the previous measurement results by MOUDI (Wang et al., 2015;Hu et al., 2012). The amount of the BC mass concentrations for the coarser mode peaks were about twice to that of the smaller mode.

The characteristic of the BCMSD was studied by fitting the shape of BCMSD with a bi-normal distribution. The relationships between the fitted D_m and GSD were statistically studied. During the aging processing, the opposite trends for the D_m and GSD were found for coarser mode. This is the first time that the coarser mode of the BCMSD were synthetically studied. The BCMSD of coarser mode varied significantly under different pollution conditions with peak diameter changed between 430 and 580 nm. However, the relationship between the D_m and GSD for smaller mode BC aerosols were more complex due to the complex sources.

When the BCMSD were changed with the polluted condition, the corresponding aerosol optical properties changes significantly. Sensitivity studies found that the aerosol g varies from 0.603 to 0.627 due to the variations in BCMSD. Aerosol g was more sensitive to D_m when the geometric mean diameter of the BCMSD is in the range of 300 nm and 370 nm. The SSA can changed from 0.90 to 0.94. The σ_{sca} experienced significant change with the variation of BCMSD from 325.6 Mm^{-1} to 364.4 Mm^{-1} and the σ_{abs} changed in the range between 24.064 Mm^{-1} and 37.27 Mm^{-1}. The corresponding BC MAC was calculated to be in the range between 5.44 and 8.08 m^2/g.

The variations in DARF were estimated due to the variations of the BCMSD by using the SBDART model. Results showed that the DARF can varies by about 8.45% for different BCMSD and the heating rate for different measured BCMSD conditions could change from 2.24 to 2.50, corresponding to a variation of 11.6%. At the same time, the variations in DARF due to the variations in the BC mixing state was estimated to be 10.5% and that of the heating rate is 8.45%. Thus, the variations of the BCMSD may had significant influence on the aerosol radiative budget and

an accurate measurement of BCMSD was very necessary.

Competing interests. The authors declare that they have no conflict of interest.

Data availability. The data used in this study is available when requesting the authors.

Author contributions. GZ, CZ, JT and YK designed and conducted the experiments; CS, YY, CZ and GZ discussed the results.

Acknowledgments. This work is supported by the National Key R&D Program of China (2016YFA0602001) and the National Natural Science Foundation of China (41590872).

References

Babu, S. S., Sreekanth, V., Moorthy, K. K., Mohan, M., Kirankumar, N. V. P., Subrahamanyam, D. B., Gogoi, M. M., Kompalli, S. K., Beegum, N., Chaubey, J. P., Kumar, V. H. A., and Manchandab, R. K.: Vertical profiles of aerosol black carbon in the atmospheric boundary layer over a tropical coastal station: Perturbations during an annular solar eclipse, Atmospheric Research, 99, 471-478, 10.1016/j.atmosres.2010.11.019, 2011.

Bau, S., Bemer, D., Grippari, F., Appert-Collin, J.-C., and Thomas, D.: Determining the effective density of airborne nanoparticles using multiple charging correction in a tandem DMA/ELPI setup, Journal of Nanoparticle Research, 16, 10.1007/s11051-014-2629-2, 2014.

Bohren, C. F., and Huffman, D. R.: Absorption and Scattering by a Sphere, in: Absorption and Scattering of Light by Small Particles, Wiley-VCH Verlag GmbH, 82-129, 2007.

Bond, T. C., Doherty, S. J., Fahey, D. W., Forster, P. M., Berntsen, T., DeAngelo, B. J., Flanner, M. G., Ghan, S., Karcher, B., Koch, D., Kinne, S., Kondo, Y., Quinn, P. K., Sarofim, M. C., Schultz, M. G., Schulz, M., Venkataraman, C., Zhang, H., Zhang, S., Bellouin, N., Guttikunda, S. K., Hopke, P. K., Jacobson, M. Z., Kaiser, J. W., Klimont, Z., Lohmann, U., Schwarz, J. P., Shindell, D., Storelvmo, T., Warren, S. G., and Zender, C. S.: Bounding the role of black carbon in the climate system: A scientific assessment, J Geophys Res-Atmos, 118, 5380-5552, 10.1002/jgrd.50171, 2013.

Cheng, Y. F., Su, H., Rose, D., Gunthe, S. S., Berghof, M., Wehner, B., Achtert, P., Nowak, A., Takegawa, N., Kondo, Y., Shiraiwa, M., Gong, Y. G., Shao, M., Hu, M., Zhu, T., Zhang, Y. H., Carmichael, G. R., Wiedensohler, A., Andreae, M. O., and Pöschl, U.: Size-resolved measurement of the mixing state of soot in the megacity Beijing, China: diurnal cycle, aging and parameterization,

Atmospheric Chemistry and Physics, 12, 4477-4491, 10.5194/acp-12-4477-2012, 2012.

Cheng, Y. H., Liao, C. W., Liu, Z. S., Tsai, C. J., and Hsi, H. C.: A size-segregation method for monitoring the diurnal characteristics of atmospheric black carbon size distribution at urban traffic sites, Atmospheric Environment, 90, 78-86, 2014.

Cheng, Y. H., and Yang, L. S.: Characteristics of Ambient Black Carbon Mass and Size-Resolved Particle Number Concentrations during Corn Straw Open-Field Burning Episode Observations at a Rural Site in Southern Taiwan, Int J Environ Res Public Health, 13, 10.3390/ijerph13070688, 2016.

China, S., Mazzoleni, C., Gorkowski, K., Aiken, A. C., and Dubey, M. K.: Morphology and mixing state of individual freshly emitted wildfire carbonaceous particles, Nature communications, 4, 2122, 2013.

Deng, Z. Z., Zhao, C. S., Ma, N., Liu, P. F., Ran, L., Xu, W. Y., Chen, J., Liang, Z., Liang, S., Huang, M. Y., Ma, X. C., Zhang, Q., Quan, J. N., Yan, P., Henning, S., Mildenberger, K., Sommerhage, E., Schafer, M., Stratmann, F., and Wiedensohler, A.: Size-resolved and bulk activation properties of aerosols in the North China Plain, Atmospheric Chemistry and Physics, 11, 3835-3846, 10.5194/acp-11-3835-2011, 2011.

Drinovec, L., Močnik, G., Zotter, P., Prévôt, A. S. H., Ruckstuhl, C., Coz, E., Rupakheti, M., Sciare, J., Müller, T., Wiedensohler, A., and Hansen, A. D. A.: The "dual-spot" Aethalometer: an improved measurement of aerosol black carbon with real-time loading compensation, Atmospheric Measurement Techniques, 8, 1965-1979, 10.5194/amt-8-1965-2015, 2015.

Ferrero, L., Mocnik, G., Ferrini, B. S., Perrone, M. G., Sangiorgi, G., and Bolzacchini, E.: Vertical profiles of aerosol absorption coefficient from micro-Aethalometer data and Mie calculation over Milan, Science of the Total Environment, 409, 2824-2837, 10.1016/j.scitotenv.2011.04.022, 2011.

Gao, R. S., Schwarz, J. P., Kelly, K. K., Fahey, D. W., Watts, L. A., Thompson, T. L., Spackman, J. R., Slowik, J. G., Cross, E. S., Han, J. H., Davidovits, P., Onasch, T. B., and Worsnop, D. R.: A Novel Method for Estimating Light-Scattering Properties of Soot Aerosols Using a Modified Single-Particle Soot Photometer, Aerosol Sci. Technol., 41, 125-135, 10.1080/02786820601118398, 2007.

Gong, X., Zhang, C., Chen, H., Nizkorodov, S. A., Chen, J., and Yang, X.: Size distribution and mixing state of black carbon particles during a heavy air pollution episode in Shanghai, Atmos. Chem. Phys., 16, 5399-5411, 10.5194/acp-16-5399-2016, 2016.

Guo, Y.: Characteristics of size-segregated carbonaceous aerosols in the Beijing-Tianjin-Hebei region, Environ. Sci. Pollut. Res., 23, 13918-13930, 10.1007/s11356-016-6538-z, 2016.

Hagen, D. E., and Alofs, D. J.: Linear Inversion Method to Obtain Aerosol Size Distributions from Measurements with a Differential Mobility Analyzer, Aerosol Sci. Technol., 2, 465-475, 10.1080/02786828308958650, 2007.

Hansen, A. D. A., Rosen, H., and Novakov, T.: The aethalometer — An instrument for the real-time measurement of optical absorption by aerosol particles, Science of The Total Environment, 36, 191-196, http://dx.doi.org/10.1016/0048-9697(84)90265-1, 1984.

He, M., and Dhaniyala, S.: A multiple charging correction algorithm for scanning electrical mobility spectrometer data, Journal of Aerosol Science, 61, 13-26, 10.1016/j.jaerosci.2013.03.007, 2013.

He, M., Dhaniyala, S., and Wagner, M.: Aerosol Filtration with Mobility-Classified Particles: Role of Multiply Charged Particles in Skewing Penetration Measurements, Aerosol Sci. Technol., 49, 704-715, 10.1080/02786826.2015.1062467, 2015.

Hu, M., Peng, J., Sun, K., Yue, D., Guo, S., Wiedensohler, A., and Wu, Z.: Estimation of size-resolved ambient particle density based on the measurement of aerosol number, mass, and chemical size distributions in the winter in Beijing, Environ Sci Technol, 46, 9941-9947, 10.1021/es204073t, 2012.

Huang, X.-F., Sun, T.-L., Zeng, L.-W., Yu, G.-H., and Luan, S.-J.: Black carbon aerosol characterization in a coastal city in South China using a single particle soot photometer, Atmospheric Environment, 51, 21-28, 10.1016/j.atmosenv.2012.01.056, 2012.

Huang, X. F., and Yu, J. Z.: Size distributions of elemental carbon in the atmosphere of a coastal urban area in South China: characteristics, evolution processes, and implications for the mixing state, Atmospheric Chemistry and Physics, 8, 5843-5853, 2008.

Jacobson, M. Z.: Strong radiative heating due to the mixing state of black carbon in atmospheric aerosols, Nature, 409, 695-697, 2001.

Janssen, N. A. H., Hoek, G., Simic-Lawson, M., Fischer, P., van Bree, L., ten Brink, H., Keuken, M., Atkinson, R. W., Anderson, H. R., Brunekreef, B., and Cassee, F. R.: Black Carbon as an Additional Indicator of the Adverse Health Effects of Airborne Particles Compared with PM10 and PM2.5, Environ Health Persp, 119, 1691-1699, 10.1289/ehp.1003369, 2011.

KlausWilleke, and Baron, P.: Aerosol measurement : principles, techniques, and applications, Van

Nostrand Reinhold, 807-808 pp., 1996.

Knutson, E. O., and Whitby, K. T.: Aerosol classification by electric mobility: apparatus, theory, and applications, Journal of Aerosol Science, 6, 443-451, 1975.

Koch, D., Schulz, M., Kinne, S., and Mcnaughton, C.: Evaluation of black carbon estimations in global aerosol models, Atmospheric Chemistry & Physics, 9, 9001-9026, 2009.

Koch, D., and Del Genio, A. D.: Black carbon semi-direct effects on cloud cover: review and synthesis, Atmos. Chem. Phys., 10, 7685-7696, 10.5194/acp-10-7685-2010, 2010.

Kuang, Y., Zhao, C. S., Tao, J. C., and Ma, N.: Diurnal variations of aerosol optical properties in the North China Plain and their influences on the estimates of direct aerosol radiative effect, Atmos. Chem. Phys., 15, 5761-5772, 10.5194/acp-15-5761-2015, 2015.

Kuang, Y., Zhao, C. S., Tao, J. C., Bian, Y. X., and Ma, N.: Impact of aerosol hygroscopic growth on the direct aerosol radiative effect in summer on North China Plain, Atmospheric Environment, 147, 224-233, 2016.

Lippmann, M., and Albert, R. E.: The Effect of Particle Size on the Regional Deposition of Inhaled Aerosols in the Human Respiratory Tract, American Industrial Hygiene Association Journal, 30, 257-275, 10.1080/00028896909343120, 1969.

Liu, D., Whitehead, J., Alfarra, M. R., Reyes-Villegas, E., Spracklen, Dominick V., Reddington, Carly L., Kong, S., Williams, Paul I., Ting, Y.-C., Haslett, S., Taylor, Jonathan W., Flynn, Michael J., Morgan, William T., McFiggans, G., Coe, H., and Allan, James D.: Black-carbon absorption enhancement in the atmosphere determined by particle mixing state, Nature Geoscience, 10, 184-188, 10.1038/ngeo2901, 2017.

Ma, N., Zhao, C. S., Müller, T., Cheng, Y. F., Liu, P. F., Deng, Z. Z., Xu, W. Y., Ran, L., Nekat, B., van Pinxteren, D., Gnauk, T., Müller, K., Herrmann, H., Yan, P., Zhou, X. J., and Wiedensohler, A.: A new method to determine the mixing state of light absorbing carbonaceous using the measured aerosol optical properties and number size distributions, Atmos. Chem. Phys., 12, 2381-2397, 10.5194/acp-12-2381-2012, 2012.

Matsui, H., Hamilton, D. S., and Mahowald, N. M.: Black carbon radiative effects highly sensitive to emitted particle size when resolving mixing-state diversity, Nature communications, 9, 3446, 10.1038/s41467-018-05635-1, 2018.

Menon, S., Hansen, J., Nazarenko, L., and Luo, Y.: Climate effects of black carbon aerosols in China

590 and India, Science, 297, 2250-2253, 10.1126/science.1075159, 2002.
591 Moffet, R. C., amp, apos, Brien, R. E., Alpert, P. A., Kelly, S. T., Pham, D. Q., Gilles, M. K., Knopf,
592 D. A., and Laskin, A.: Morphology and mixing of black carbon particles collected in central
593 California during the CARES field study, Atmospheric Chemistry and Physics, 16, 14515-14525,
594 10.5194/acp-16-14515-2016, 2016.
595 Moteki, N., and Kondo, Y.: Dependence of Laser-Induced Incandescence on Physical Properties of
596 Black Carbon Aerosols: Measurements and Theoretical Interpretation, Aerosol Sci. Technol., 44,
597 663-675, Pii 924375405
598 10.1080/02786826.2010.484450, 2010.
599 Nichols, J. L., Owens, E. O., Dutton, S. J., and Luben, T. J.: Systematic review of the effects of black
600 carbon on cardiovascular disease among individuals with pre-existing disease, International Journal
601 of Public Health, 58, 707-724, 2013.
602 Ning, Z., Chan, K. L., Wong, K. C., Westerdahl, D., Močnik, G., Zhou, J. H., and Cheung, C. S.:
603 Black carbon mass size distributions of diesel exhaust and urban aerosols measured using differential
604 mobility analyzer in tandem with Aethalometer, Atmospheric Environment, 80, 31-40,
605 10.1016/j.atmosenv.2013.07.037, 2013.
606 Ohata, S., Moteki, N., and Kondo, Y.: Evaluation of a Method for Measurement of the Concentration
607 and Size Distribution of Black Carbon Particles Suspended in Rainwater, Aerosol Sci. Technol., 45,
608 1326-1336, 2011.
609 Peng, J., Hu, M., Guo, S., Du, Z., Zheng, J., Shang, D., Levy Zamora, M., Zeng, L., Shao, M., Wu,
610 Y.-S., Zheng, J., Wang, Y., Glen, C. R., Collins, D. R., Molina, M. J., and Zhang, R.: Markedly
611 enhanced absorption and direct radiative forcing of black carbon under polluted urban environments,
612 Proceedings of the National Academy of Sciences, 201602310, 10.1073/pnas.1602310113, 2016.
613 Peng, J., Hu, M., Guo, S., Du, Z., Shang, D., Zheng, J., Zheng, J., Zeng, L., Shao, M., Wu, Y., Collins,
614 D., and Zhang, R.: Ageing and hygroscopicity variation of black carbon particles in Beijing
615 measured by a quasi-atmospheric aerosol evolution study (QUALITY) chamber, Atmospheric
616 Chemistry and Physics, 17, 10333-10348, 10.5194/acp-17-10333-2017, 2017.
617 Raatikainen, T., Brus, D., Hooda, R. K., Hyvärinen, A.-P., Asmi, E., Sharma, V. P., Arola, A., and
618 Lihavainen, H.: Size-selected black carbon mass distributions and mixing state in polluted and clean
619 environments of northern India, Atmospheric Chemistry and Physics, 17, 371-383,

10.5194/acp-17-371-2017, 2017.
Ramachandran, S., and Rajesh, T. A.: Black carbon aerosol mass concentrations over Ahmedabad, an urban location in western India: Comparison with urban sites in Asia, Europe, Canada, and the United States, J Geophys Res-Atmos, 112, Artn D06211
10.1029/2006jd007488, 2007.
Ramanathan, V., and Carmichael, G.: Global and regional climate changes due to black carbon, Nature Geoscience, 1, 221-227, 10.1038/ngeo156, 2008.
Ran, L., Deng, Z., Xu, X., Yan, P., Lin, W., Wang, Y., Tian, P., Wang, P., Pan, W., and Lu, D.: Vertical profiles of black carbon measured by a micro-aethalometer in summer in the North China Plain, Atmospheric Chemistry and Physics, 16, 10441-10454, 10.5194/acp-16-10441-2016, 2016a.
Ran, L., Deng, Z. Z., Wang, P. C., and Xia, X. A.: Black carbon and wavelength-dependent aerosol absorption in the North China Plain based on two-year aethalometer measurements, Atmospheric Environment, 142, 132-144, 10.1016/j.atmosenv.2016.07.014, 2016b.
Reddington, C. L., McMeeking, G., Mann, G. W., Coe, H., Frontoso, M. G., Liu, D., Flynn, M., Spracklen, D. V., and Carslaw, K. S.: The mass and number size distributions of black carbon aerosol over Europe, Atmospheric Chemistry and Physics, 13, 4917-4939, 10.5194/acp-13-4917-2013, 2013.
Ricchiazzi, P., Yang, S., Gautier, C., and Sowle, D.: SBDART: A Research and Teaching Software Tool for Plane-Parallel Radiative Transfer in the Earth's Atmosphere, Bulletin of the American Meteorological Society, 79, 2101-2114, 10.1175/1520-0477(1998)079<2101:sarats>2.0.co;2, 1998.
Roberts, G. C., Ramana, M. V., Corrigan, C., Kim, D., and Ramanathan, V.: Simultaneous observations of aerosol-cloud-albedo interactions with three stacked unmanned aerial vehicles, Proceedings of the National Academy of Sciences of the United States of America, 105, 7370-7375, 10.1073/pnas.0710308105, 2008.
Schwarz, J. P., Gao, R. S., Fahey, D. W., Thomson, D. S., Watts, L. A., Wilson, J. C., Reeves, J. M., Darbeheshti, M., Baumgardner, D. G., Kok, G. L., Chung, S. H., Schulz, M., Hendricks, J., Lauer, A., Kärcher, B., Slowik, J. G., Rosenlof, K. H., Thompson, T. L., Langford, A. O., Loewenstein, M., and Aikin, K. C.: Single-particle measurements of midlatitude black carbon and light-scattering aerosols from the boundary layer to the lower stratosphere, Journal of Geophysical Research, 111, 10.1029/2006jd007076, 2006.
Singh, S., Fiddler, M. N., and Bililign, S.: Measurement of size-dependent single scattering albedo of

650 fresh biomass
651 burning aerosols using the extinction-minus-scattering technique with a
652 combination of cavity ring-down spectroscopy and nephelometry, Atmospheric Chemistry and
653 Physics, 16, 13491-13507, 10.5194/acp-16-13491-2016, 2016.
654 Song, S., Wu, Y., Xu, J., Ohara, T., Hasegawa, S., Li, J., Yang, L., and Hao, J.: Black carbon at a
655 roadside site in Beijing: Temporal variations and relationships with carbon monoxide and particle
656 number size distribution, Atmospheric Environment, 77,
657 213-221, https://doi.org/10.1016/j.atmosenv.2013.04.055, 2013.
658 Stabile, L., Fuoco, F. C., and Buonanno, G.: Characteristics of particles and black carbon emitted by
659 combustion of incenses, candles and anti-mosquito products, Building and Environment, 56, 184-191,
660 10.1016/j.buildenv.2012.03.005, 2012.
661 Stevens, B., and Feingold, G.: Untangling aerosol effects on clouds and precipitation in a buffered
662 system, Nature, 461, 607-613, 10.1038/nature08281, 2009.
663 Tigges, L., Wiedensohler, A., Weinhold, K., Gandhi, J., and Schmid, H. J.: Bipolar charge
664 distribution of a soft X-ray diffusion charger, Journal of Aerosol Science, 90, 77-86,
665 10.1016/j.jaerosci.2015.07.002, 2015.
666 Turner, M. D., Henze, D. K., Hakami, A., Zhao, S. L., Resler, J., Carmichael, G. R., Stanier, C. O.,
667 Baek, J., Sandu, A., Russell, A. G., Nenes, A., Jeong, G. R., Capps, S. L., Percell, P. B., Pinder, R. W.,
668 Napelenok, S. L., Bash, J. O., and Chai, T. F.: Differences Between Magnitudes and Health Impacts
669 of BC Emissions Across the United States Using 12 km Scale Seasonal Source Apportionment,
670 Environmental Science & Technology, 49, 4362-4371, 10.1021/es505968b, 2015.
671 Venkataraman, C., and Friedlander, S. K.: Size distributions of polycyclic aromatic hydrocarbons and
672 elemental carbon. 2. Ambient measurements and effects of atmospheric processes, Environmental
673 Science & Technology, 28, 563, 1994.
674 Virkkula, A., Makela, T., Hillamo, R., Yli-Tuomi, T., Hirsikko, A., Hameri, K., and Koponen, I. K.: A
675 simple procedure for correcting loading effects of aethalometer data, J Air Waste Manag Assoc, 57,
676 1214-1222, 10.3155/1047-3289.57.10.1214, 2007.
677 Virkkula, A., Chi, X., Ding, A., Shen, Y., Nie, W., Qi, X., Zheng, L., Huang, X., Xie, Y., Wang, J.,
678 Petaja, T., and Kulmala, M.: On the interpretation of the loading correction of the aethalometer,
679 Atmospheric Measurement Techniques, 8, 4415-4427, 10.5194/amt-8-4415-2015, 2015.

Wang, Q. Y., Huang, R. J., Cao, J. J., Tie, X. X., Ni, H. Y., Zhou, Y. Q., Han, Y. M., Hu, T. F., Zhu, C. S., Feng, T., Li, N., and Li, J. D.: Black carbon aerosol in winter northeastern Qinghai–Tibetan Plateau, China: the source, mixing state and optical property, Atmospheric Chemistry and Physics, 15, 13059-13069, 10.5194/acp-15-13059-2015, 2015.

Wex, H., Neusüß, C., Wendisch, M., Stratmann, F., Koziar, C., Keil, A., Wiedensohler, A., and Ebert, M.: Particle scattering, backscattering, and absorption coefficients: An in situ closure and sensitivity study, Journal of Geophysical Research: Atmospheres, 107, LAC 4-1-LAC 4-18, 10.1029/2000jd000234, 2002.

Wiedensohler, A.: An approximation of the bipolar charge distribution for particles in the submicron size range, Journal of Aerosol Science, 19, 387-389, 1988.

Wiedensohler, A., and Fissan, H. J.: Aerosol charging in high purity gases, Journal of Aerosol Science, 19, 867-870, 1988.

Wilcox, E. M., Thomas, R. M., Praveen, P. S., Pistone, K., Bender, F. A. M., and Ramanathan, V.: Black carbon solar absorption suppresses turbulence in the atmospheric boundary layer, Proceedings of the National Academy of Sciences, 113, 11794-11799, 10.1073/pnas.1525746113, 2016.

Wu, Y., Cheng, T., Zheng, L., and Chen, H.: Effect of morphology on the optical properties of soot aggregated with spheroidal monomers, Journal of Quantitative Spectroscopy & Radiative Transfer, 168, 158-169, 2016a.

Wu, Y., Wang, X., Tao, J., Huang, R., Tian, P., Cao, J., Zhang, L., Ho, K.-F., and Zhang, R.: Size distribution and source of black carbon aerosol in
urban Beijing during winter haze episodes, Atmospheric Chemistry and Physics Discussions, 1-25, 10.5194/acp-2016-1096, 2016b.

Wu, Y., Cheng, T., Liu, D., Allan, J. D., Zheng, L., and Chen, H.: Light Absorption Enhancement of Black Carbon Aerosol Constrained by Particle Morphology, Environ Sci Technol, 52, 6912-6919, 10.1021/acs.est.8b00636, 2018.

Yu, H., and Yu, J. Z.: Modal Characteristics of Elemental and Organic Carbon in an Urban Location in Guangzhou, China, Aerosol Sci. Technol., 43, 1108-1118, 2009.

Yu, H., Wu, C., Wu, D., and Yu, J. Z.: Size distributions of elemental carbon and its contribution to light extinction in urban and rural locations in the pearl river delta region, China, Atmos. Chem. Phys., 10, 5107-5119, 10.5194/acp-10-5107-2010, 2010.

Zhang, R., Khalizov, A. F., Pagels, J., Zhang, D., Xue, H., and McMurry, P. H.: Variability in morphology, hygroscopicity, and optical properties of soot aerosols during atmospheric processing, Proceedings of the National Academy of Sciences of the United States of America, 105, 10291-10296, 10.1073/pnas.0804860105, 2008.

Zhang, Y., Zhang, Q., Cheng, Y., Su, H., Kecorius, S., Wang, Z., Wu, Z., Hu, M., Zhu, T., Wiedensohler, A., and He, K.: Measuring the morphology and density of internally mixed black carbon with SP2 and VTDMA: new insight into the absorption enhancement of black carbon in the atmosphere, Atmospheric Measurement Techniques, 9, 1833-1843, 10.5194/amt-9-1833-2016, 2016.

Zhang, Y., Su, H., Kecorius, S., Wang, Z., Hu, M., Zhu, T., He, K., Wiedensohler, A., Zhang, Q., and Cheng, Y.: Mixing State of Refractory Black Carbon of the North China Plain
Regional Aerosol Combining a Single Particle Soot Photometer and
a Volatility Tandem Differential Mobility Analyzer, Atmospheric Chemistry and Physics Discussions, 1-27, 10.5194/acp-2017-222, 2017.

Zhang, Y., Zhang, Q., Cheng, Y., Su, H., Li, H., Li, M., Zhang, X., Ding, A., and He, K.: Amplification of light absorption of black carbon associated with air pollution, Atmospheric Chemistry and Physics, 18, 9879-9896, 10.5194/acp-18-9879-2018, 2018.

Zhao, G., Zhao, C., Kuang, Y., Bian, Y., Tao, J., Shen, C., and Yu, Y.: Calculating the aerosol asymmetry factor based on measurements from the humidified nephelometer system, Atmospheric Chemistry and Physics, 18, 9049-9060, 10.5194/acp-18-9049-2018, 2018.

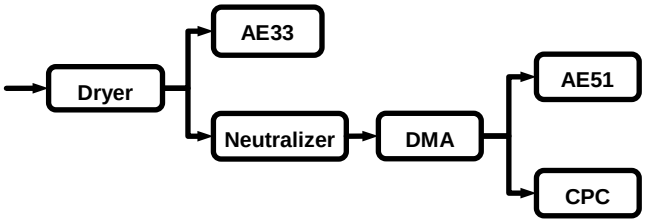

731

732 **Figure 1.** The schematic diagram of the instrument setup.

733

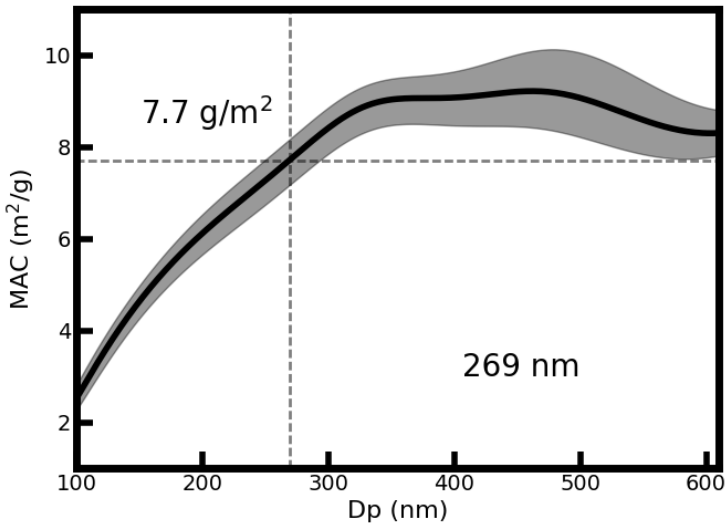

734

735 **Figure 2.** Calculated mass absorption coefficient of different aerosol.

736

737

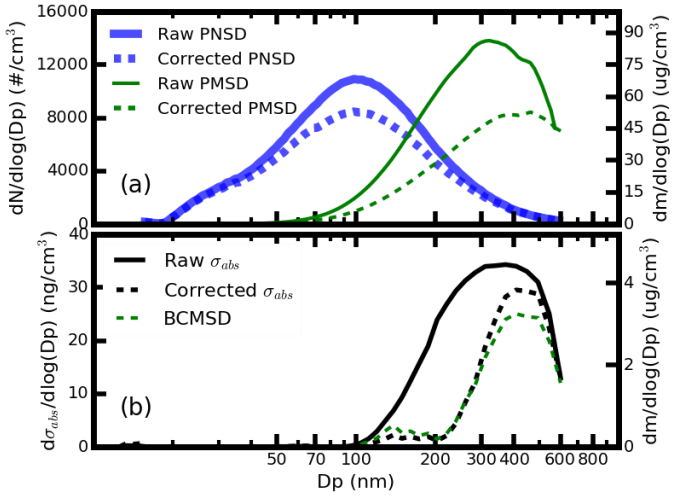

738

739 **Figure 3.** Case of multiple charging correction processing. (a) the multiple charging correction of the
740 aerosol PNSD and aerosol PMSD, (b) the multiple charging correction of the size-resolved σ_{abs}.
741 The solid line is the measured results without multiple charging corrections and the dotted line is the
742 multiple charging corrections results.

743

744

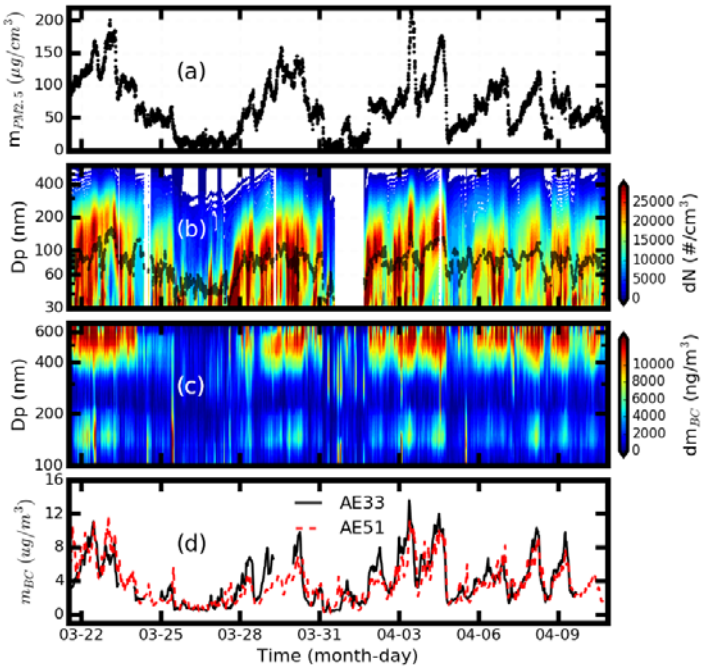

745

746 **Figure 4.** The measured time series of mass concentrations for (a) the PM2.5; (b) the aerosol
747 PNSD in filled color, the geometric median diameter in dotted line;(c) the BCMSD and (d) the
748 m_{BC} by AE33 (black) and m_{BC} from integrated BCMSD from AE51 (red).

749

750

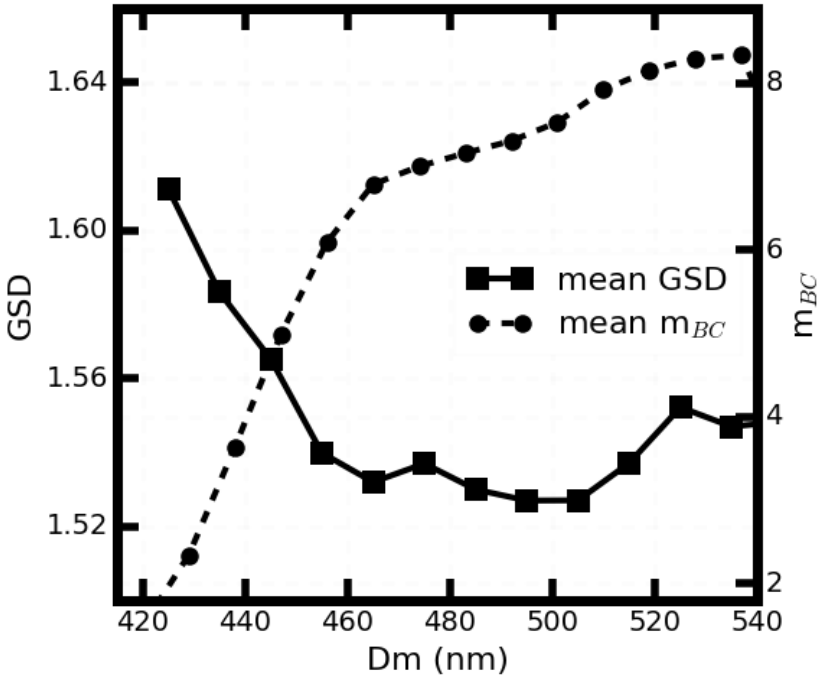

Figure 5. The relationship between the Dm and the GSD. The black dots show the real measured Dm and GSD. The black line shows the mean results of the GSD for different Dm. The black line marked with square shows the variation of mean m_{BC} with the Dm.

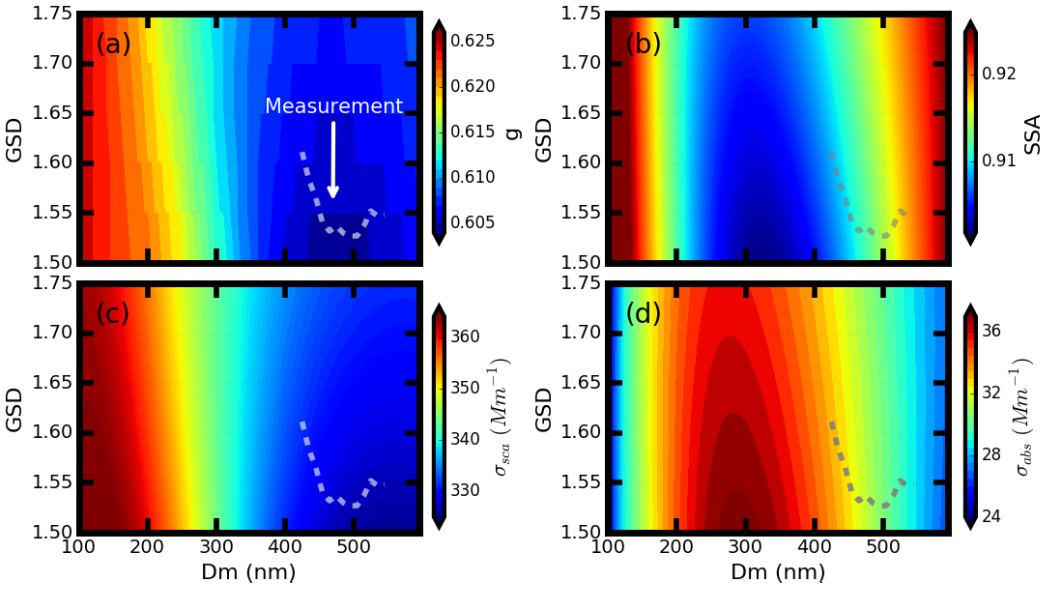

Figure 6. Variations of aerosol optics properties using the measured mean aerosol PNSD and m_{BC} under different BCMSD conditions, which are represented by different Dm and GSD values: (a) aerosol asymmetry factor, (b) single scatter albedo, (c) scattering coefficient and (d) extinction coefficient . The grey dotted line in the figure shows the evolution path of the BCMSD according to results of field measurements.

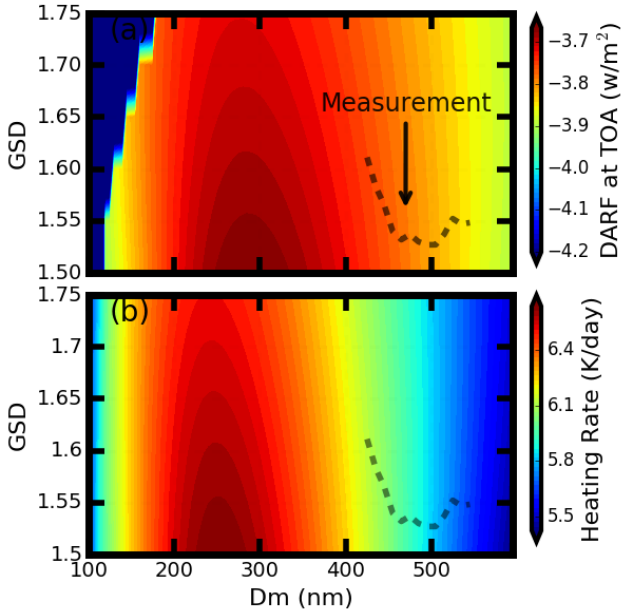

Figure 7. Variations of (a) DARF and (b) heating rate under different BCMSD conditions, which are represented by different Dm and GSD values. The black dotted line in the figure shows the evolution path of the BCMSD according to results of field measurements.

768 **Table 1.** Comparison of the DARF and heating rate values under different BC mixing states and
769 different BCMSD conditions.

		Mixing State			BCMSD	
		Internal	**External**	**Core-Shell**	**Minimum**	**Maximum**
DARF	**Value(w/m^2)**	**-3.45**	**-3.56**	**-3.81**	**-3.97**	**-3.67**
	Variation	**10.5%**			**8.45%**	
Heat Rate	**Value(K/day)**	**2.51**	**2.32**	**2.53**	**2.24**	**2.50**
	Variation	**9.71%**			**11.6%**	

770